ACS OMEGA

Article

Cite This: ACS Omega 2018, 3, 11624−11632

http://pubs.acs.org/journal/acsodf

Crystal and Magnetic Structures of La_2CoPtO_6 Double Perovskite

Sanghyun Lee,[†] Min-Cheol Lee,[‡,§] Yoshihisa Ishikawa,[†,∥] Ping Miao,[†,∥] Shuki Torii,[†,⊥] Choongjae Won,[#] Kyungdong Lee,[#] Namjung Hur,[#] Deok-Yong Cho,*[,¶] and Takashi Kamiyama*[,†,∥,⊥]

[†]Institute of Materials Structure Science, [∥]Sokendai(The Graduate University for Advanced Studies), and [⊥]J-PARC Center, KEK, Tokai 319-1106, Japan

[‡]Center for Correlated Electron Systems, Institute for Basic Science (IBS), Seoul 08826, Korea

[§]Department of Physics and Astronomy, Seoul National University, Seoul 08826, Korea

[#]Department of Physics, Inha University, Incheon 22212, Korea

[¶]IPIT and Department of Physics, Chonbuk National University, Jeonju 54896, Korea

ABSTRACT: We investigated the crystal structure and magnetic structure in cobaltite-platinate double perovskite of La_2CoPtO_6, employing various techniques of X-ray diffraction, neutron diffraction, and the extended X-ray absorption fine structure analysis. It is shown that the crystal symmetry is maintained as $P2_1/n$ in the temperature range of <500 °C, whereas the lattice constants and the Co−Co distances undergo a continuous structural evolution toward the high-symmetry phases with increasing temperature. The Co−O bonds were overall longer and had a larger degree of structural and thermal disorders than the Pt−O bonds. As for the magnetism, an antiferromagnetic order is stabilized in the Co^{2+} sublattice at temperatures below 28 K. It is demonstrated that owing to the substantial distortions (quantified by a distortion parameter $\Sigma > 0.03$ Å) of the Co−Co networks, the system is not subject to spin frustration effect. Details in the magnetic structure are determined; at 12 K, the Co magnetic moment was (0.8, 0, 2.7) Bohr magneton, the magnetic propagation vector was (−0.5, 0, 0.5), and the magnetic symmetry was preferably $\Gamma_1(A_g)$.

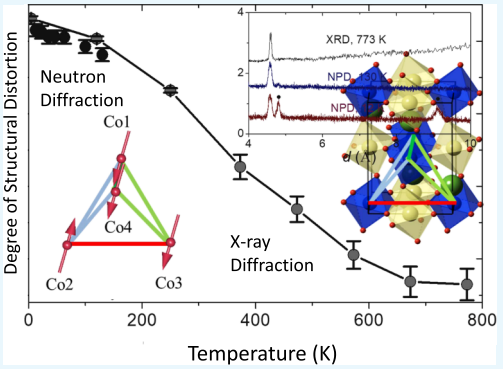

1. INTRODUCTION

Double perovskite (DP) $A_2BB'O_6$ (A: alkali or rare-earth ions and B/B′: transition-metal ions) has drawn attention because of its various electronic and/or magnetic functionalities including half metallicity for spintronics,[1,2] multiferroicity,[3,4] or photocatalysis.[5] Compared to simple perovskite ABO_3, the inherent disproportionation of charges and spins in the alternatingly mixed B and B′ sites can allow us to control such multifunctionality by choosing the ionic species for the B/B′ site.[1,2] Of particular interest would be to explore a new crystal structure and/or spin ordering in artificially engineered compositions.[1,2,6]

When B and B′ ions in DP interact strongly with each other, magnetism in DP is driven predominantly by the B−B′ interaction. For instance, in the case of Sr_2FeMoO_6, a ferromagnetic order is stabilized by the nonlocal interaction between the d electrons in Fe^{2+} and Mo^{4+} (ref 2). However, when either one is inactive (i.e., nonmagnetic), the interaction among the B ions within the sublattice mostly determines the magnetic order in spite of the long B−B distance (typically above 5 Å).

In a perfect high-symmetry DP (for the schematic, see the left panel in Figure 1), B and B′ sublattices constitute the NaCl-like double face-centered-cubic (fcc) structure.[7,8] It has been reported in many DPs having inactive B′ that ordering of the B spins tends to be frustrated because of the symmetric geometry in the fcc network.[9−11] However, when the structural distortion is significant, the fcc network can become

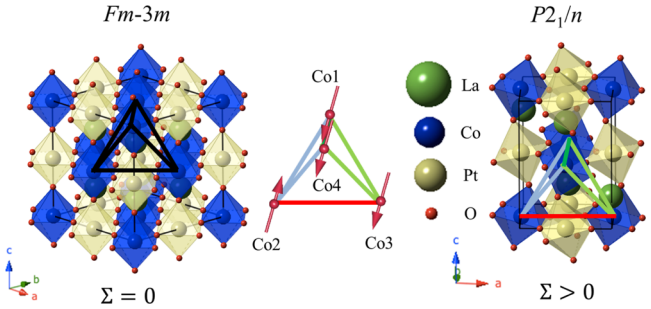

Figure 1. Crystal structure of La_2CoPtO_6 double perovskite ($P2_1/n$, right) and the aristo-type double perovskite ($Fm\bar{3}m$, no distortion, left). The actual crystal (right) undergoes the structural distortions so as to unequalize the Co−Co distances in the tetrahedral network (middle). The arrows on the vertices of the tetrahedron show the directions of the 4 Co magnetic moments exemplarily following the $\Gamma_1(A_g)$ model. Σ, the variance of the six Co−Co bond lengths, is used as a measure of distortion of the tetrahedral network. The spin frustration effects can be suppressed when $\Sigma > 0$.

Received: July 18, 2018
Accepted: September 10, 2018
Published: September 21, 2018

DOI: 10.1021/acsomega.8b01701
ACS Omega 2018, 3, 11624−11632

asymmetric, and thus, the magnetic order can be reinstated.[12,13] Indeed, it has been observed in DPs with various A ions that the spin ordering is associated with the structural distortion, which is tunable due to different ionic sizes of the A site ions.[1]

This study focused on examining the structure and magnetic orders of a novel platinate DP, La_2CoPtO_6. Structural study on platinate DP has been rarely reported so far, simply because of the difficulty in the synthesis.[14,15] We chose La_2CoPtO_6 to study the magnetism of the Co spins. Compared to the high-symmetry DPs such as cubic Ba_2YRuO_6 ($Fm\bar{3}m$; ref 9) or tetragonal Sr_2CoOsO_6 ($I4/m$; refs 16 and 17), in which spin orders in Ru or Co ions are frustrated, La_2CoPtO_6 has a distorted crystal structure ($P2_1/n$), which might stabilize the magnetism in the sublattices of B−B′ sites.

It was shown in our previous reports[18,19] that the oxidation number of Pt is +4, whereas that of Co is +2 in La_2CoPtO_6. Because the total spin of Pt 5d electrons should be null, only the spin interaction between the Co^{2+} ions can dominate the magnetic ordering. Also, Co^{2+} ions are prone to show a peculiar magnetoelastic property because of strong spin−orbit coupling.[20] Furthermore, to the extent of our knowledge, there have been no reports on the magnetic structure of platinate DPs. Therefore, we studied in details the crystal structure and the spin ordering in novel La_2CoPtO_6 using various techniques for structural identification: X-ray diffraction (XRD) for crystal structure, extended X-ray absorption fine structure (EXAFS) analyses for local structures of Co/Pt, and neutron diffraction (ND) for the magnetic structure at low temperature.

2. RESULTS AND DISCUSSION

2.1. Crystal Structure. Figure 1 shows the crystal structure of La_2CoPtO_6. As in many other double perovskites,[1,7] the crystal symmetry of La_2CoPtO_6 was determined to be monoclinic ($P2_1/n$, right panel), that is, lowered from $Fm\bar{3}m$ for aristo-type DP (left panel) due to octahedral rotations and distortions. The results of the XRD analyses (Figures 2 and 3) show that the $P2_1/n$ symmetry is preserved up to at least 773 K, suggesting persistent structural distortions even at temperatures far above the room temperature.

In regard to the magnetism of the double perovskite, particular interest is on the network of the 4 Co spins depicted in the figure. Because La or Pt has no spin magnetic moments, the magnetism is determined solely by the intersite interactions of the Co 3d. The Co ions occupy the fcc sublattices, so they interact with each other through the network of indirect Co−Co bonds (with bond lengths ∼5.6 Å), which comprises the edge-sharing tetrahedra. The intersite interactions are dominated by the superexchange interactions, favoring an antiferromagnetic coupling (spins tend to be aligned in the opposite directions). The exchanges between each of the 4 Co ions [Coi (i = 1−4)] are denoted by $J_{\mathrm{Co}i-\mathrm{Co}j}$'s (>0). Generally, $J_{\mathrm{Co-Co}}$ increases as the Co−Co distance decreases.

In the $Fm\bar{3}m$ structure, the bond lengths of the six edges in the tetrahedron (shown in Figure 1) are all identical and so are the $J_{\mathrm{Co-Co}}$'s. Under the circumstance, the 4 Co spins in the tetrahedron (shown in the middle of Figure 1) cannot be aligned antiparallel all together. Instead, at least one of them should align parallel, which might suppress the magnetic order. This is the spin frustration effect in the case of ideally symmetric fcc network.

On the other hand, in the actual monoclinic crystal ($P2_1/n$), the tetrahedron is distorted so as to possess 4 different Co−Co bond lengths; 4 out of 6 bond lengths forms two pairs of bonds with the same length. For instance, Co1−Co2 and Co4−Co2 bonds form a pair of bonds with an identical length, and Co1−Co3 and Co4−Co3 bonds form the other pair of bonds. The bonds are colored in Figure 1 according to the bond lengths. A good measure to quantify the degree of the tetrahedral distortion is the variance of the six bond lengths ($\Sigma = \sqrt{\sum_{i<j}^{4}[(d_{ij} - \langle d\rangle)^2/6]}$), where d_{ij} is the distance between Coi and Coj and $\langle d\rangle$ is the average. As Σ increases, the asymmetry of the tetrahedron and the resultant inequality in $J_{\mathrm{Co-Co}}$'s become severe. This suggests that a preferential spin orientation can be settled, breaking up the spin frustration when Σ > 0 under the tetrahedral distortion in the $P2_1/n$ symmetry.

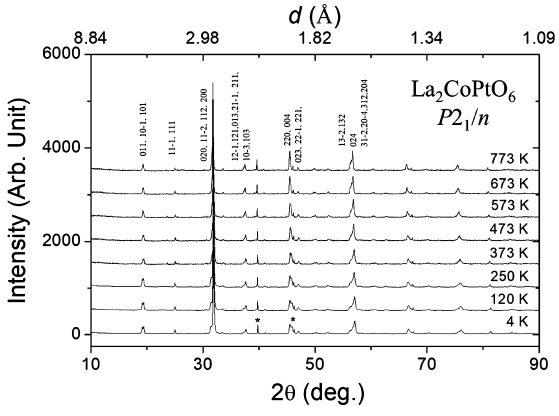

Figure 2. XRD data taken at temperatures from 4 to 773 K. The $P2_1/n$ symmetry is preserved for all of the temperatures. The asterisks show the signature of segregated Pt (less than 3% of the sample). Miller indices (hkl)'s according to the $P2_1/n$ symmetry are given in the figure.

2.2. X-ray Diffraction. In order to identify the crystal structure of La_2CoPtO_6, XRD was carried out at various temperatures. Figure 2 shows the XRD patterns taken at 4−773 K. Overall peaks can be assigned to the (hkl) reflections according to the $P2_1/n$ symmetry, except for the small contribution of segregated Pt (<3%), which is irrelevant to the double perovskite. As the temperature increases, some of the peaks [for instance, (220) and (024)] appear to merge and become more intense. We checked a possibility of phase transition into higher crystal symmetry. Upon the continuous structural phase transition, the monoclinic $P2_1/n$ group can be derived only from either $C2/m$ or $P4/mnc$ supergroup.[7] Therefore, it is probable to undergo a continuous transition to the higher symmetry structures with increasing temperature. However, the two groups are not consistent with the presence of (11−1)/(111) peak near $2\theta = 25°$, which exists at all the temperatures, as shown in Figure 2. Therefore, we can tell that the crystal symmetry of La_2CoPtO_6 is maintained as $P2_1/n$ for all the temperatures.

Then, the apparent merging of peaks at high temperatures can be understood as the signature of a continuous symmetrization of the lattices while preserving the $P2_1/n$ symmetry. Figure 3 shows the structure parameters obtained from the XRD results. The unit cell volume V, the lattice constants in pseudo-cubic notations a_{pc}, and the monoclinic angle β are displayed in Figure 3a−c, respectively. With increasing temperature, the three lattice constants tend to

DOI: 10.1021/acsomega.8b01701
ACS Omega 2018, 3, 11624−11632

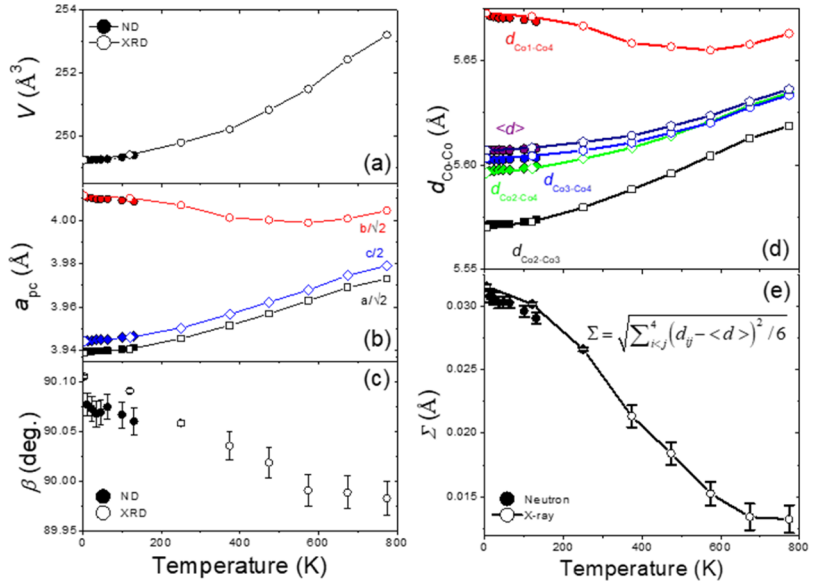

Figure 3. Structural parameters determined by XRD (4−773 K) together with ND (≤130 K): (a) unit cell volume V, (b) lattice constants in pseudo-cubic notations (a_{pc}), and (c) monoclinic angle β. (d) Distances between the four Co ions, that is, the vertices in the tetrahedron shown in Figure 1. (e) Variance of the Co−Co bond lengths ($\Sigma = \sqrt{\sum_{i<j}^{4}[(d_{ij} - \langle d\rangle)^2/6]}$) as a measure of the distortion of the Co tetrahedron. The large values of Σ's (>0.03 Å) at low temperatures suggest a substantial distortion of the Co tetrahedral networks, which can break up the frustration condition for the Co spin order.

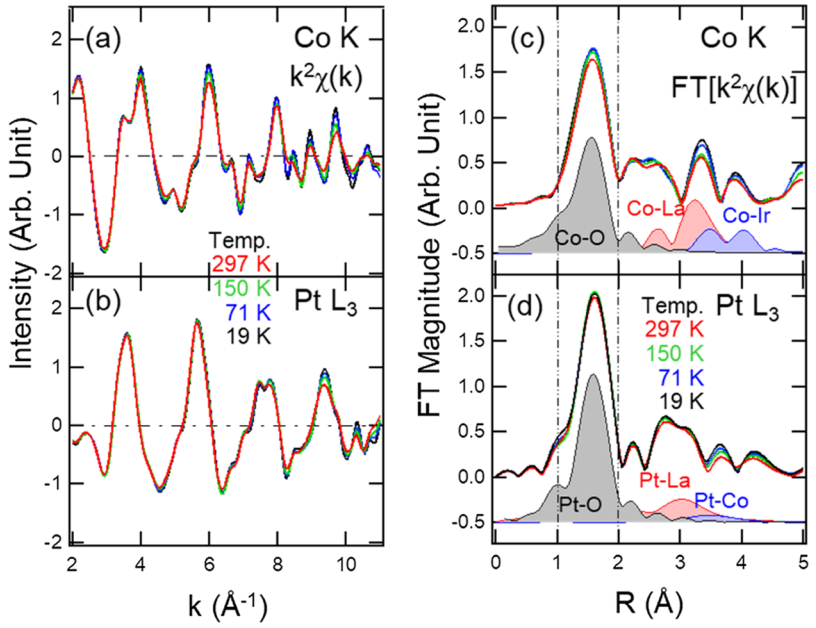

Figure 4. (a) Co K-edge and (b) Pt L_3-edge EXAFS oscillations $\chi(k)$ weighted by k^2 at various temperatures. The magnitudes of their FT data are displayed with the simulated FT EXAFSs for Co(Pt)−O/La/Pt(Co) in (c,d). The bond lengths appear to be almost constants of temperature, whereas the peak intensities decrease with increasing temperature because of thermal disorders in bond lengths. The horizontal dashed lines in (a,b) are guides for the eyes, and the vertical dashed lines in (c,d) show the R range for the disorder analyses in Figure 5.

become similar to each other and β approaches to 90°. This reflects a continuous thermal evolution of the crystal structure toward a higher-entropy phase (but still preserving the $P2_1/n$ symmetry).

Because Co and Pt occupy 2*c* and 2*d* special positions in the $P2_1/n$ symmetry, respectively, d_{ij} values can be calculated directly from the values of a_{pc} and β. Figure 2d,e shows, respectively, the d_{ij}'s and Σ at various temperatures. All of the d_{ij}'s tend to increase as the temperature increases because of thermal expansion. Their variance, Σ decreases again reflecting a continuous structural evolution toward the high-symmetry phases. For comparison, the data obtained by the ND (Figures 7 and 8) are appended for the respective figures in Figure 3. The results from ND are very consistent with those from XRD.

It is noteworthy that at low temperature, the value of Σ becomes saturated to the highest value (0.0308 Å) (see Table 2). We can tell that the temperature evolution of Σ is significant, in that it increases two times as temperature

DOI: 10.1021/acsomega.8b01701
ACS Omega 2018, 3, 11624−11632

decreases (773 K → 12 K). The substantial structural distortion can hinder the spin frustration allowing a long-ranged magnetism at low temperature, which is indeed the case in La_2CoPtO_6.

2.3. Extended X-Ray Absorption Fine Structure. Generally, atomic structures estimated by diffraction techniques are described in reciprocal space so that only the structures of atoms that are arranged periodically can be identified. Thus, it is rather difficult to directly observe short-ranged orders or instant vibration of chemical bonds and so forth. Meanwhile, such local structural information, complementary to the information on long-ranged orders, can be provided by EXAFS. In the EXAFS analyses, oscillatory fine structures ($\chi(k)$) in the higher energy region in the X-ray absorption spectroscopy (XAS) spectra are deduced as functions of the final-state electron momentum (k). Furthermore, Fourier transformation (FT) of the $\chi(k)$'s provides the real space information on the atomic arrangements near the photon absorbing atom with respect to the phase uncorrected interatomic distance R. The signals from each of the atomic species can be collected separately by selecting the edges (or the range of photon energies used in the XAS measurement).

Figure 4 shows the $\chi(k)$'s multiplied by k^2 obtained at (a) Co K- and (b) Pt L_3-edges. The horizontal dashed lines are the guides for the eyes, indicating the zero values. Overall, the line shapes and positions of crests and troughs in $\chi(k)$'s are almost independent of the measurement temperature. Meanwhile, the amplitudes of $\chi(k)$'s decreases with increasing temperature particularly at high k's. This can be attributed to the structural or thermal disorders (σ^2) in the coordination [$\chi(k) \propto \exp(-2k^2\sigma^2)$].

The FT magnitudes at Co K- and Pt L_3-edges are shown as functions of R in Figure 4c,d, respectively. The FT was processed on $k^2\chi(k)$ within a k range of 2−10 $Å^{-1}$. The FT magnitudes in Figure 4c,d show overall information of the bonding of Co and Pt, respectively, on the order of increasing bond length. The peaks can be assigned to bonds according to R's; the main peaks near R = 1.5 Å can be attributed to the Co/Pt−O bonds, whereas the smaller peaks at higher R's can be attributed to the bonds with adjacent La or Pt/Co. For clear peak assignments, the simulated FT spectra for Co−O, Co−La, and Co−Pt single scatterings are appended in Figure 4c and those for Pt−O, Pt−La, and Pt−Co are done in Figure 4d, as well. It is shown that the features of Co(Pt)−La/Pt(Co) overlap with each other and are likely masked by the FT ripples as well as by the contributions of the multiple scatterings, such as Co−O−O−Co or Pt−O−La−Pt. This hinders an accurate peak assignment for the higher R region (>2 Å).

The R values of the Co/Pt−O bonding appear to be almost constants of temperature, suggesting that the average bond lengths hardly change with temperature at least below room temperature. However, the peak intensities gradually decrease with increasing temperature. This indicates the increase of the values of σ^2's because the coordination number of Co−O and Pt−O is fixed as 6 under the $P2_1/n$ crystal structure.

Figure 5 shows the values of σ^2's for Co−O and Pt−O bonds obtained by fitting the first shell peaks (R = 1−2 Å as highlighted by the vertical dashed lines in Figure 4b) at various temperatures. Note that the values of σ^2's would correspond to the variance in bond length in the direction of −O bonds. If we presume that the oxygen ions are frozen (without any structural disorders), the values should be comparable with the B_{iso} values obtained by the Rietveld refinement of the ND data (in Table 1) divided by $8\pi^2$. The σ^2's for Co−O are somewhat large (~0.010 Å) compared to those for Pt−O (~0.006 Å). This might be relevant to a minute site-to-site variation in the atomic position of Co^{2+} ions, which are subject to a magnetostriction effect due to spin−orbit coupling.[20] As the temperature increases, the σ^2's for Co−O increase noticeably, whereas those for Pt−O remains almost constant. The selective increase of σ^2's can be attributed to the fact that the mass of Co^{2+} ion should be smaller than that of Pt^{4+} ion; the lighter ion would vibrate more easily than the heavier ion.

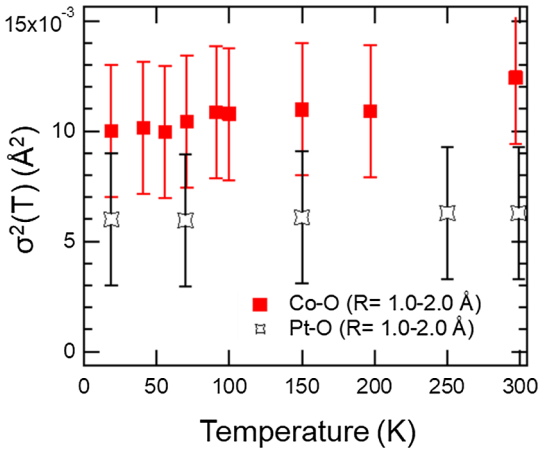

Figure 5. Parameter for structural disorders in average Co−O and Pt−O bond lengths (σ^2), estimated by EXAFSs from the first shells (with R range of 1.0−2.0 Å). The σ^2's for Co−O are overall larger and increase more rapidly with increasing temperature than those for Pt−O for all of the temperatures.

2.4. Magnetism. Magnetic susceptibility ($\chi_m = M/H$) of La_2CoPtO_6 is displayed in Figure 6 as a function of temperature. The specimen was first cooled down without external magnetic field (H; namely, zero-field cooling), then χ_m was measured under H = 5000 Oe. The cusp in the χ_m curve suggests existence of an antiferromagnetic order with a Néel temperature (T_N) of 28 K. The reciprocal ($1/\chi_m$) is also shown in the inset. The extrapolation from the slope at the high-temperature range (200−400 K) to the abscissa shows that the Weiss temperature (Θ) is ~−28 K. The effective magnetic moment μ_{eff} is estimated to be approximately 4.72 μ_B, which is larger than the value from the spin-only value of 2 $\sqrt{S(S+1)}\mu_B = 3.87\mu_B$ for S = 3/2. The increment in μ_{eff} might reflect the contribution of unquenched orbital moment because of distortion of the CoO_6 octahedra. The ratio $f = |\Theta|/T_N$ is 1, which implies that the spins are not frustrated in La_2CoPtO_6.

2.5. Neutron Diffraction. Figure 7a shows the t.o.f. ND patterns at low temperatures (≤130 K). Besides the peaks from the crystal structures (persistent for all of the temperatures), magnetic peaks emerge near d = 4.8 Å and d = 9.1 Å at temperatures below 35 K. In the inset, the diffraction patterns in 12 and 130 K data are shown together to highlight their correlation with the antiferromagnetic order. The magnetic peaks are assigned to $(hkl)_m$ = (±0.5, 1, −0.5) and (−0.5, 0, ±0.5), respectively, where the magnetic indices $(hkl)_m$ are the sum of the nuclei's indices $(hkl)_n$ and the indices for the magnetic propagation vector $\vec{K}$. $\vec{K}$ is defined as the reciprocals of the periodicity of the magnetic moments; for incidence, the

DOI: 10.1021/acsomega.8b01701
ACS Omega 2018, 3, 11624−11632

Table 1. Structural Parameters of La_2CoPtO_6 Obtained by the Rietveld Refinement on the Neutron Powder Diffraction Data from the 90° Bank[a]

temperature (K)	12 K	23 K	46 K	100 K	130 K
a (Å)	5.5713(2)	5.5713(2)	5.5715(2)	5.5727(2)	5.5738(2)
b (Å)	5.6716(2)	5.6712(2)	5.6706(2)	5.6696(2)	5.6689(2)
c (Å)	7.8883(3)	7.8889(3)	7.8899(3)	7.8917(3)	7.8932(3)
β (degree)	90.08(1)	90.07(1)	90.07(1)	90.07(1)	90.06(1)
V (Å^3)	249.25(2)	249.26(2)	249.27(2)	249.34(2)	249.40(2)
La x	0.5097(6)	0.5093(6)	0.5097(6)	0.5093(6)	0.5096(6)
La y	0.5533(3)	0.5532(3)	0.5533(3)	0.5530(3)	0.5528(3)
La z	0.2508(7)	0.2508(7)	0.2505(7)	0.2507(7)	0.2502(7)
O1 x	0.2151(8)	0.2149(9)	0.2149(9)	0.2148(9)	0.2147(8)
O1 y	0.2012(9)	0.2010(9)	0.2009(9)	0.2009(9)	0.2016(9)
O1 z	0.9622(9)	0.9613(10)	0.9618(10)	0.9625(9)	0.9625(9)
O2 x	0.3027(8)	0.3027(9)	0.3022(9)	0.3022(9)	0.3022(8)
O2 y	0.7103(9)	0.7100(9)	0.7106(9)	0.7103(9)	0.7099(9)
O2 z	0.9519(8)	0.9524(9)	0.9517(9)	0.9514(9)	0.9512(8)
O3 x	0.4168(6)	0.4168(6)	0.4168(6)	0.4168(6)	0.4172(6)
O3 y	0.9846(4)	0.9843(5)	0.9845(5)	0.9848(5)	0.9841(4)
O3 z	0.2533(9)	0.2530(9)	0.2525(9)	0.2532(9)	0.2529(9)
B_{iso}La (Å^2)	0.04(4)	0.07(4)	0.07(4)	0.07(4)	0.12(4)
BisoCo/Pt (Å$_2$)	0.95(5)	0.92(5)	0.92(5)	1.01(5)	0.98(5)
B_{iso}O (Å$_2$)	0.48(4)	0.46(4)	0.50(4)	0.52(4)	0.50(3)
Co_a (μ_B)	0.8(1)	0.6(1)			
Co_b (μ_B)	0[b]	0[b]			
Co_c (μ_B)	2.7(1)	2.2(1)			
Co (μ_B)	2.8(1)	2.2(1)			
R_p (%)	6.04	6.26	6.21	6.15	5.70
R_{wp} (%)	8.44	8.60	8.52	8.43	8.05
R_{exp} (%)	2.97	3.40	3.40	3.40	2.26
χ^2 (%)	8.05	6.38	6.28	6.13	12.70

[a]We used $\Gamma_1(A_g)$ magnetic model with the magnetic propagation vector (−0.5, 0, 0.5). Co occupies 2c positions: (0, 1/2, 0) and (1/2, 0,1/2), and Pt occupies 2d positions: (1/2, 0, 0) and (0, 1/2, 1/2). O1 and O2 atoms interconnect the Co and Pt in the ab plane, whereas O3 atoms do along the c axis. [b]Co_b is set to 0 during the refinement so as to obtain the most reliable results.

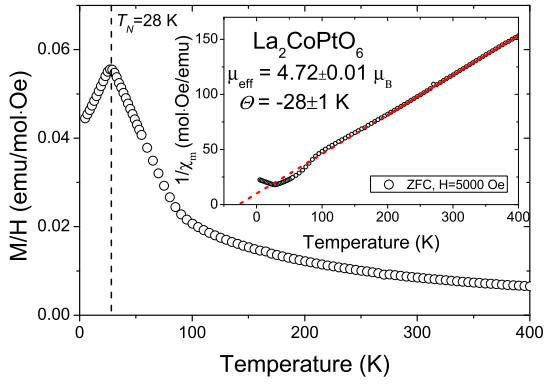

Figure 6. Magnetic susceptibility ($\chi_m = M/H$) with an external magnetic field of H = 5000 Oe, measured after the zero-field cooling. The cusp in the χ_m curve shows the antiferromagnetic order with a Néel temperature (T_N) of 28 K. The reciprocal ($1/\chi_m$) is shown in the inset, and the extrapolation from the slope at high-temperature range to the abscissa shows that the Weiss temperature (Θ) is ∼−28 K. Thus, the ratio $f = |\Theta|/T_N \approx 1$. This implies the absence of spin frustration effects in La_2CoPtO_6.

magnetic propagation vector in La_2CoPtO_6 is determined to be (−1/2, 0, 1/2) in this work (see the spin structures in Figure 9), that is, the same spins can be found at sites generated by a translation vector (−2a, 0, 2c).

The peak intensities of the two magnetic peaks are plotted as functions of temperature in Figure 7b. Seeing the sudden increase in intensity at temperature near 28 K as the temperature decreases, it is obvious that those peaks are indeed relevant to the antiferromagnetic order. The results of the Rietveld refinement on the ND data are summarized in Figure 8 and Tables 1 and 2. Figure 8 shows the (a) Co−O and (b) Pt−O bond lengths and (c) the Co−O−Pt bond angles at low temperatures. Although the lengths of bonds to oxygen are all different from each other, they are almost constants of temperature in the temperature range, suggesting rigidity in the structural distortion ($P2_1/n$).

It should be noted that the average bond length of Co−O is larger than that of Pt−O in spite of much smaller atomic number. This can be attributed mainly to smaller valence of Co^{2+} in comparison to Pt^{4+}. The Co−O1 and Co−O2 bond lengths are found to be almost identical, whereas that of Co−O3 is approximately 0.1 Å smaller, constituting CoO_6 octahedra of a D_{4h}-like point symmetry shortened along the c axis. On the other hand, the lengths of the Pt−O1, O2, and O3 bonds are all different from each other but the differences are not severe. The bigger size and anisotropy in CoO_6 might be related to the larger disorders in Co−O bonds shown in the results of the EXAFS analyses (Figures 4 and 5).

Table 1 shows the structural parameters for several temperatures. Co occupies 2c positions [(0, 1/2, 0) and (1/2, 0,1/2)], and Pt occupies 2d positions [(1/2, 0, 0) and (0, 1/

DOI: 10.1021/acsomega.8b01701
ACS Omega 2018, 3, 11624−11632

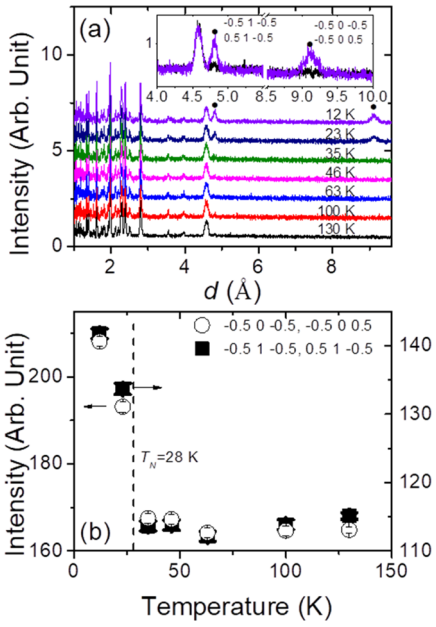

Figure 7. (a) ND patterns at low temperatures (≤130 K). Besides the peaks from the crystal structures, magnetic peaks emerge near d = 4.8 Å and d = 9.1 Å at temperatures below ∼28 K. In the inset, the diffraction patterns in the 12 and 130 K data are shown together to highlight their magnetic origins. The magnetic peaks are assigned to $(hkl)_m$ = (±0.5, 1, −0.5) and (−0.5, 0, ±0.5). (b) Peak intensities of the two magnetic peaks at various temperatures.

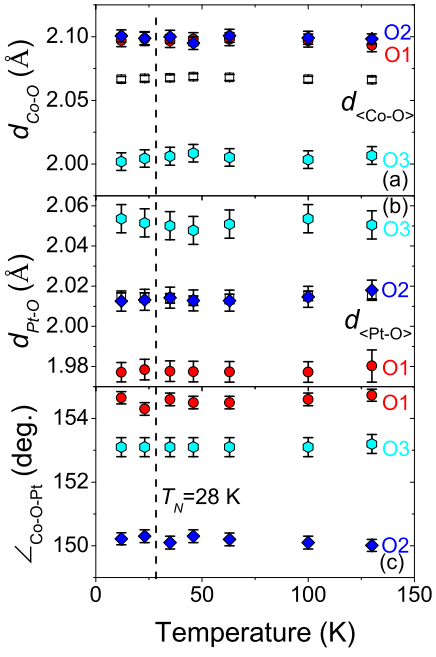

Figure 8. (a) Co−O and (b) Pt−O bond lengths and (c) Co−O−Pt bond angles at low temperatures from the ND data. No significant structural change is observed upon increasing the temperature.

2, 1/2)]. There are three oxygen sites; O1 and O2 atoms connect the Co and Pt atoms in *ab* plane, whereas O3 atoms do along *c* axis. The magnetic moments at Co sites [(Co_*a*, Co_*b*, Co_*c*)] are also determined. The magnetic moment of Co^{2+} at 12 K was estimated to be (0.8, 0, 2.7) μ_B with a total magnetic moment of 2.8 μ_B. The y value of the magnetic moment is so small (<0.3 μ_B) as to hinder to obtain a reliable value. Thus, we fixed Co_b = 0 within our magnetic models during Rietveld refinement. The B_{iso}'s represent the isotropic terms for the thermal ellipsoid, comparable with the σ^2's obtained from the EXAFS analysis (Figure 5).

Bond lengths, angles, and the distortion parameter Σ (defined in Figures 1 and 3) at given temperatures are listed in Table 2. Being related to the spin frustration, the fact that Σ is maximized at low temperatures (see Figure 3e) implies that the structural distortions are substantial at low temperature, which, in turn, can allow the system to have a preferred magnetic order. Thereby, the frustration effects of the Co spins can be suppressed in La_2CoPtO_6.

The complete magnetic structure can be obtained by measuring the magnetic propagation vector and the magnetic point symmetry. The former tells the periodicity of the magnetic moments over the unit cell, whereas the latter does the relationship between the two Co ions (in 2*c* positions in $P2_1/n$) in the same unit cell. It is shown by the Rietveld refinement that the magnetic propagation vector is (−0.5, 0, 0.5). According to the magnetic symmetry analysis, there are two magnetic structure candidates for Co sites under the magnetic propagation vector; they are $\Gamma_1(A_g)$ and $\Gamma_3(B_g)$. $\Gamma_1(A_g)$ dictates that if the magnetic moment at (0, 0.5, 0) is (M_a, M_b, M_c), that at (0.5, 0, 0.5) should be $(-M_a, M_b, -M_c)$, namely, a ferromagnetic ordering along *b* axis and an antiferromagnetic ordering along *a* axis and/or *c* axis within the crystal unit cell. On the contrary, in the case of $\Gamma_3(B_g)$, the magnetic moment at (0.5, 0, 0.5) should be $(M_a, -M_b, M_c)$ instead, so that an antiferromagnetic ordering along *b* axis and a ferromagnetic ordering along *a* axis and/or *c* axis within the crystal unit cell. Despite the ferromagnetic ordering between the magnetic moments at (0, 0.5, 0) and (0.5, 0, 0.5), the net magnetic moment over the magnetic unit cell must be zero for both the $\Gamma_1(A_g)$ and $\Gamma_3(B_g)$ symmetries because the translations either by (*a*, 0, 0) or (0, 0, *c*) will cancel out all of the magnetic moments due to the magnetic propagation vector (−0.5, 0, 0.5).

The results of the Rietveld refinement for the 12 K data are plotted in Figure 9. For the determination of the magnetic structures, we used the 30° band data instead of the 90° bank data because it covers a broader *d* range, which is needed for the analysis of the magnetic peaks with longer periodicity. The upper (lower) left panels show the experimental ND pattern and the theoretical pattern calculated based on the $\Gamma_1(A_g)$ ($\Gamma_3(B_g)$) model. The magnetic structures of the two models are appended in the right panels beside their respective ND patterns. Except for the difference highlighted by the arrows in the insets, the theoretical ND patterns appear very similar to each other. Therefore, the quality of the fit (R_{mag}) of $\Gamma_1(A_g)$ is only slightly better than that of $\Gamma_3(B_g)$.

This suggests that it is difficult to unequivocally judge from the experimental data that only the $\Gamma_1(A_g)$ symmetry prevails. If the two models indeed coexisted, they presumably reside in different magnetic domains. Possible coexistence of $\Gamma_1(A_g)$ and $\Gamma_3(B_g)$ might suggest that ambiguity could still remain in determining the spin directions for all of the Co sites even in the presence of long-ranged antiferromagnetic order at 12 K (below T_N).

Nevertheless, we can tell that the $\Gamma_1(A_g)$ model is slightly more favored as the magnetic ground state. The preference of the $\Gamma_1(A_g)$ model can be rationalized by considering the exchange interactions of the 4 Co spins in the tetrahedral networks as in Figure 1. Suppose the *b* axis components of the

DOI: 10.1021/acsomega.8b01701
ACS Omega 2018, 3, 11624−11632

Table 2. Bond Lengths, Bond Angles, and the Distortion Parameters (Co−Co Distances) in Figures 3 and 8[a]

	temperature (K)				
	12 K	23 K	46 K	100 K	130 K
Bond Lengths					
Co−O1 (Å)	2.097(5)	2.098(5)	2.098(5)	2.097(5)	2.093(5)
Co−O2 (Å)	2.101(5)	2.099(5)	2.095(5)	2.099(5)	2.098(4)
Co−O3 (Å)	2.002(7)	2.004(7)	2.008(7)	2.003(7)	2.007(7)
⟨Co−O⟩ (Å)	2.067(2)	2.067(2)	2.069(2)	2.067(2)	2.066(2)
Pt−O1 (Å)	1.977(5)	1.979(5)	1.978(5)	1.977(5)	1.980(5)
Pt−O2 (Å)	2.013(5)	2.013(5)	2.013(5)	2.015(5)	2.018(5)
Pt−O3 (Å)	2.054(7)	2.052(7)	2.048(7)	2.054(7)	2.051(7)
⟨Pt−O⟩ (Å)	2.015(2)	2.014(2)	2.013(2)	2.015(2)	2.016(2)
Bond Angles					
∠Co−O1−Pt (deg)	154.7(2)	154.3(2)	154.5(2)	154.6(2)	154.7(2)
∠Co−O2−Pt (deg)	150.2(2)	150.3(2)	150.3(2)	150.1(2)	150.0(2)
∠Co−O3−Pt (deg)	153.1(3)	153.1(3)	153.1(3)	153.1(3)	153.2(3)
Co Tetrahedron (Figure 1)					
Co1−Co4 (Å)	5.5713(2)	5.5713(2)	5.5715(2)	5.5727(2)	5.5738(2)
Co2−Co3 (Å)	5.6716(2)	5.6712(2)	5.6706(2)	5.6696(2)	5.6689(2)
Co2−Co4(Å)	5.5972(4)	5.5974(4)	5.5978(4)	5.5986(4)	5.5994(4)
Co3−Co4 (Å)	5.6024(4)	5.6024(4)	5.6025(4)	5.6032(4)	5.6035(4)
⟨Co−Co⟩ (Å)	5.6070(1)	5.6070(1)	5.6071(1)	5.6076(1)	5.6081(1)
Σ (Å)	0.0308(4)	0.0306(4)	0.0303(4)	0.0296(4)	0.0291(4)

[a]The Co2−Co4 (=Co1−Co2) distance is $\frac{\sqrt{(a+c\cos\beta)^2+b^2+(c\sin\beta)^2}}{2}$, and the Co3−Co4 (=Co1−Co3) distance is $\frac{\sqrt{(a-c\cos\beta)^2+b^2+(c\sin\beta)^2}}{2}$.

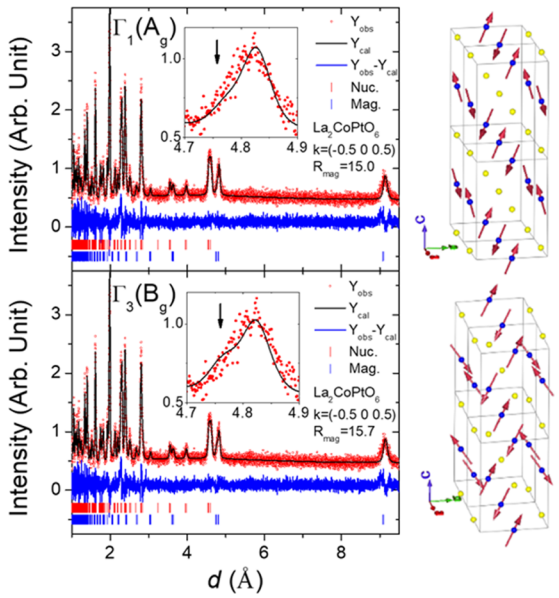

Figure 9. Magnetic structure at 12 K from the 30° bank. The magnetic propagation vectors were found to be (−0.5, 0, 0.5), and the magnetic symmetry defining the relative orientations among the adjacent magnetic moments is preferably $\Gamma_1(A_g)$ rather than $\Gamma_3(B_g)$. The two spin orders are displayed in the right panels. The insets and the arrows highlight the small differences between the calculated ND patterns. See the text for more details.

Co magnetic moments (Co_*b* in Table 1) are negligible. Three out of 4 (Co1, Co4, and Co3) has the same directions, whereas Co2 has the opposite direction. Because of the magnetic propagation vector of (−0.5, 0, 0.5), the spins of Co2 and Co3 should be antiparallel to each other and those of Co1 and Co4 should also be parallel to each other (see Figure 1).

However, the relative orientations between Co1 (Co4) and Co2 (or Co3) are not deterministic, but they can change delicately depending on the competing two superexchange interactions (favoring antiparallel spin alignments) of $J_{Co2-Co4}$ and $J_{Co3-Co4}$. If $J_{Co2-Co4}$ is larger than $J_{Co3-Co4}$, Co2 should align antiparallel to Co1 and Co4 and then Co3 should align parallel unfavorably. On the contrary, if $J_{Co3-Co4}$ is larger than $J_{Co2-Co4}$, Co3 aligns antiparallel and then Co2 should align parallel. The strength of exchange interaction is closely related to the Co−Co distance; stronger exchange interaction for shorter bonds.

It is shown in Figure 3 and Table 2, the Co2−Co4 (=Co2−Co1) distance is slightly shorter than the Co3−Co4 (=Co3−Co1) for all of the temperatures because the monoclinic angle β slightly exceeds 90°. This suggests that $J_{Co2-Co4}$ is larger than $J_{Co3-Co4}$, so that the 4 Co magnetic moments follow the $\Gamma_1(A_g)$ model (as depicted in the middle panel of Figure 1). On the other hand, in the $\Gamma_3(B_g)$ model, the directions of magnetic moments on Co2 and Co3 should be reversed, which is unfavorable. Therefore, it is very reasonable for the Co spins to prefer the $\Gamma_1(A_g)$ symmetry.

It is noteworthy that although a probability of existence of the $\Gamma_3(B_g)$ symmetry is not excluded experimentally, the antiferromagnetic order over the unit cells is clearly determined as $\vec{K}$ = (−0.5, 0, 0.5) with expanding the magnetic unit cells by 2 × 1 × 2 below the Néel temperature. In this regard, we can tell that the magnetic order is not frustrated (f = 1) in the cobaltite-platinate DP.

3. CONCLUSIONS

Combined XRD + ND + EXAFS study revealed the crystal and magnetic structures of La_2CoPtO_6 in details. Although the crystal symmetry is maintained as $P2_1/n$ at least up to 773 K, the lattice parameters tend to become symmetrized with increasing temperature, suggesting a continuous structural evolution toward high-symmetry phases. The Co−O bonds were overall longer and had a larger degree of structural and thermal disorders than the Pt−O bonds. As for the magnetism,

DOI: 10.1021/acsomega.8b01701
ACS Omega 2018, 3, 11624−11632

an antiferromagnetic order is stabilized in the Co^{2+} sublattice at $T < 28$ K, with the magnetic moment $M_{Co} = (0.8, 0, 2.7)\ \mu_B$ (at 12 K), the magnetic propagation vector of (−0.5, 0, 0.5), and the magnetic symmetry of $\Gamma_1(A_g)$ (preferentially). Substantial degree of structural distortions in the tetrahedral Co networks ($\Sigma > 0.03$ Å) can explain the absence of spin frustration effect ($|\Theta|/T_N = 1$) and the resultant antiferromagnetic ordering in La_2CoPtO_6.

4. EXPERIMENTAL/MATERIALS AND METHODS

A La_2CoPtO_6 powder sample was prepared by a solid-state reaction method.[18] A mixture of La_2O_3, Co_3O_4, and PtO_2 was sintered at 900−1150 °C for several days with intermediate grinding. It is observed in the XRD and ND data that a small amount of Pt (<3%) were segregated. However, the average valence of Pt is 4 + predominantly,[19] suggesting that the segregation effects hardly alter the chemistry or crystal structure of main double perovskite.

XRD was conducted at various temperatures (4−773 K) using Rigaku SmartLab (Cu $K\alpha_1$). The t.o.f. neutron powder diffraction was carried out at temperatures below 130 K on ∼4 g of the specimen in the SuperHRPD beamline in J-PARC.[21,22] The space group and lattice constants are determined from both the XRD and ND data.

For the analyses of the XRD and ND data, we employed Z-Rietveld[23,24] and Fullprof.[25] The atomic coordinates and the bond information including Pt−O bond lengths or Co−O−Pt bond angles were obtained by processing the Rietveld refinement on the ND data collected from the 90° bank. For the magnetic structure analyses, the data were collected from the 30° bank and the symmetry analyses were performed employing SARAH program.[26]

For the EXAFS analyses, hard XAS was performed at the 17C1 beamline in Taiwan Light Source in the transmission mode. The EXAFS procedures including the background removal and the FT were undergone using UWXAFS package.[27] The magnetic susceptibility was measured by using a SQUID magnetometer (Quantum Design) in CROSS-Tokai.

AUTHOR INFORMATION

Corresponding Authors

*E-mail: zax@jbnu.ac.kr. Phone: +82 63270 3444 (D.-Y.C.).
*E-mail: takashi.kamiyama@kek.jp. Phone: +81 29 864 5612 (T.K.).

ORCID

Deok-Yong Cho: 0000-0001-5789-8286

Author Contributions

D.-Y.C. and S.L. designed the study. S.L., Y.I., P.M., and S.T. performed the neutron and X-ray diffractions, and M.-C.L. and D.-Y.C. conducted the EXAFS analyses. C.W., K.L., and N.H. prepared the samples. D.-Y.C. and T.K. supervised the research. The manuscript was written through contributions of all authors.

Notes

The authors declare no competing financial interest.

ACKNOWLEDGMENTS

The ND experiment using the SuperHRPD beamline was carried out under general user program 2015A0318 and S-type project 2014S05. D.-Y.C. was supported by Basic Science Research Program through the National Research Foundation of Korea (NRF) funded by the Ministry of Education (NRF-2018R1D1A1B07043427) and by National R&D Program through the NRF funded by the Ministry of Science, ICT and Future Planning (NRF-2017K1A3A7A09016305). S.L. was supported by JSPS KAKENHI grant number JP16K17758. The magnetic susceptibility measurement was under the support at the CROSS user laboratory. We appreciate M. Hagihala for helpful discussion, M. Shioya and K. Shimizu for technical supports in the ND experiment, and T. Moyoshi for assistance in the magnetic susceptibility measurement.

REFERENCES

(1) Vasala, S.; Karppinen, M. A2B′B″O6 perovskites: A review. *Prog. Solid State Chem.* **2015**, *43*, 1−36.
(2) Serrate, D.; De Teresa, J. M.; Ibarra, M. R. Double perovskites with ferromagnetism above room temperature. *J. Phys.: Condens. Matter* **2006**, *19*, 023201.
(3) Azuma, M.; Takata, K.; Saito, T.; Ishiwata, S.; Shimakawa, Y.; Takano, M. Designed ferromagnetic, ferroelectric Bi_2NiMnO_6. *J. Am. Chem. Soc.* **2005**, *127*, 8889−8892.
(4) Chikara, S.; Singleton, J.; Bowlan, J.; Yarotski, D. A.; Lee, N.; Choi, H. Y.; Zapf, V. S. Electric polarization observed in single crystals of multiferroic Lu_2MnCoO_6. *Phys. Rev. B* **2016**, *93*, No. 180405(R).
(5) Kanhere, P.; Chen, Z. A review on visible light active perovskite-based photocatalysts. *Molecules* **2014**, *19*, 19995−20022.
(6) Hossain, A.; Bandyopadhyay, P.; Roy, S. An overview of double perovskites $A_2B'B''O_6$ with small ions at A site: Synthesis, structure and magnetic properties. *J. Alloys Compd.* **2018**, *740*, 414−427.
(7) Howard, C. J.; Kennedy, B. J.; Woodward, P. M. Ordered double perovskites—a group-theoretical analysis. *Acta Crystallogr., Sect. B: Struct. Sci.* **2003**, *59*, 463−471.
(8) Balachandran, P. V.; Rondinelli, J. M. Interplay of octahedral rotations and breathing distortions in charge-ordering perovskite oxides. *Phys. Rev. B: Condens. Matter Mater. Phys.* **2013**, *88*, 054101.
(9) Aharen, T.; Greedan, J. E.; Ning, F.; Imai, T.; Michaelis, V.; Kroeker, S.; Zhou, H.; Wiebe, C. R.; Cranswick, L. M. D. Magnetic properties of the S= 3/2 geometrically frustrated double perovskites La_2LiRuO_6 and Ba_2YRuO_6. *Phys. Rev. B: Condens. Matter Mater. Phys.* **2009**, *80*, 134423.
(10) Carlo, J. P.; Clancy, J. P.; Fritsch, K.; Marjerrison, C. A.; Granroth, G. E.; Greedan, J. E.; Dabkowska, H. A.; Gaulin, B. D. Spin gap and the nature of the $4d^3$ magnetic ground state in the frustrated fcc antiferromagnet Ba_2YRuO_6. *Phys. Rev. B: Condens. Matter Mater. Phys.* **2013**, *88*, 024418.
(11) Kermarrec, E.; Marjerrison, C. A.; Thompson, C. M.; Maharaj, D. D.; Levin, K.; Kroeker, S.; Granroth, G. E.; Flacau, R.; Yamani, Z.; Greedan, J. E.; Gaulin, B. D. Frustrated fcc antiferromagnet Ba_2YOsO_6: structural characterization, magnetic properties, and neutron scattering studies. *Phys. Rev. B: Condens. Matter Mater. Phys.* **2015**, *91*, 075133.
(12) Bernardo, P. L.; Ghivelder, L.; Amorim, H. S.; Neumeier, J. J.; García, S. Magnetic structure driven by monoclinic distortions in the double perovskite Sr_2YRuO_6. *New J. Phys.* **2015**, *17*, 103007.
(13) Aczel, A. A.; Bugaris, D. E.; Li, L.; Yan, J.-Q.; De la Cruz, C.; zur Loye, H.-C.; Nagler, S. E. Frustration by competing interactions in the highly distorted double perovskites $La_2NaB'O_6$ (B′= Ru, Os). *Phys. Rev. B: Condens. Matter Mater. Phys.* **2013**, *87*, 014435.
(14) Ouchetto, K.; Archaimbault, F.; Choisnet, J.; Et-Tabirou, M. New ordered and distorted perovskites: the mixed platinates Ln_2MPtO_6 (Ln= La, Pr, Nd, Sm, Eu, Gd; M= Mg, Co, Ni, Zn). *Mater. Chem. Phys.* **1997**, *51*, 117−124.
(15) Yamada, I.; Takahashi, Y.; Ohgushi, K.; Nishiyama, N.; Takahashi, R.; Wada, K.; Kunimoto, T.; Ohfuji, H.; Kojima, Y.; Inoue, T.; Irifune, T. $CaCu_3Pt_4O_{12}$: The First Perovskite with the B site Fully Occupied by Pt4+. *Inorg. Chem.* **2010**, *49*, 6778−6780.
(16) Paul, A. K.; Reehuis, M.; Felser, C.; Abdala, P. M.; Jansen, M. Synthesis, Crystal Structure, and Properties of the Ordered Double Perovskite Sr_2CoOsO_6. *Z. Anorg. Allg. Chem.* **2013**, *639*, 2421.

DOI: 10.1021/acsomega.8b01701
ACS Omega 2018, 3, 11624−11632

(17) Yan, B.; Paul, A. K.; Kanungo, S.; Reehuis, M.; Hoser, A.; Többns, D. M.; Schnelle, W.; Williams, R. C.; Lancaser, T.; Xiao, F.; Möllr, J. S.; Blundell, S. J.; Hayes, W.; Felser, C.; Jansen, M. Lattice-Site-Specific Spin Dynamics in Double Perovskite Sr_2CoOsO_6. *Phys. Rev. Lett.* **2014**, *112*, 147202.
(18) Lee, M.-C.; Sohn, C. H.; Kim, S. Y.; Lee, K. D.; Won, C. J.; Hur, N.; Kim, J.-Y.; Cho, D.-Y.; Noh, T. W. Stabilization of ferromagnetic ordering in cobaltite double perovskites of La_2CoIrO_6 and La_2CoPtO_6. *J. Phys.: Condens. Matter* **2015**, *27*, 336002.
(19) Lee, M.-C.; Lee, S.; Won, C. J.; Lee, K. D.; Hur, N.; Chen, J.-L.; Cho, D.-Y.; Noh, T. W. Hybridized orbital states in spin-orbit coupled 3d− 5d double perovskites studied by x-ray absorption spectroscopy. *Phys. Rev. B* **2018**, *97*, 125123.
(20) Lee, S.; Ishikawa, Y.; Miao, P.; Torii, S.; Ishigaki, T.; Kamiyama, T. Magnetoelastic coupling forbidden by time-reversal symmetry: Spin-direction-dependent magnetoelastic coupling on MnO, CoO, and NiO. *Phys. Rev. B* **2016**, *93*, 064429.
(21) Torii, S.; Yonemura, M.; Yulius Surya Panca Putra, T.; Zhang, J.; Miao, P.; Muroya, T.; Tomiyasu, R.; Morishima, T.; Sato, S.; Sagehashi, H.; Noda, Y.; Kamiyama, T. Super High Resolution Powder Diffractometer at J-PARC. *J. Phys. Soc. Jpn.* **2011**, *80*, SB020.
(22) Torii, S.; Yonemura, M.; Ishikawa, Y.; Miao, P.; Tomiyasu, R.; Satoh, S.; Noda, Y.; Kamiyama, T. Improvement of Instrument Devices for Super High Resolution Powder Diffractometer at J-PARC. *J. Phys.: Conf. Ser.* **2014**, *502*, 012052.
(23) Oishi, R.; Yonemura, M.; Nishimaki, Y.; Torii, S.; Hoshikawa, A.; Ishigaki, T.; Morishima, T.; Mori, K.; Kamiyama, T. Rietveld analysis software for J-PARC. *Nucl. Instrum. Methods Phys. Res., Sect. A* **2009**, *600*, 94−96.
(24) Oishi-Tomiyasu, R.; Yonemura, M.; Morishima, T.; Hoshikawa, A.; Torii, S.; Ishigaki, T.; Kamiyama, T. Application of matrix decomposition algorithms for singular matrices to the Pawley method inZ-Rietveld. *J. Appl. Crystallogr.* **2012**, *45*, 299−308.
(25) Rodríguez-Carvajal, J. Recent advances in magnetic structure determination by neutron powder diffraction. *Phys. B* **1993**, *192*, 55−69.
(26) Wills, A. S. A new protocol for the determination of magnetic structures using simulated annealing and representational analysis (SARAh). *Phys. B* **2000**, *276-278*, 680−681.
(27) Stern, E. A.; Newville, M.; Ravel, B.; Yacoby, Y.; Haskel, D. The UWXAFS analysis package: philosophy and details. *Phys. B* **1995**, *208-209*, 117−120.

DOI: 10.1021/acsomega.8b01701
ACS Omega 2018, 3, 11624−11632